

# The Binary Black Hole Model for Mrk 231 Cannot Explain the Observed Emission Lines

Karen M. Leighly<sup>1</sup>

*Homer L. Dodge Department of Physics and Astronomy, The University of Oklahoma, 440 W. Brooks St., Norman, OK 73019*

Donald M. Terndrup

*Department of Astronomy, The Ohio State University, 140 W. 18th Ave., Columbus, OH 43210*

Sarah C. Gallagher

*Department of Physics & Astronomy and Centre for Planetary and Space Exploration, The University of Western Ontario, London, ON, N6A 3K7, Canada*

Adrian B. Lucy

*Department of Astronomy, Columbia University, 550 W. 120th Street, New York, NY 10027*

## ABSTRACT

Mrk 231 is a nearby quasar with an unusually red continuum, generally explained as heavy reddening by dust (e.g., Leighly et al. 2014). Yan et al. (2015) proposed that Mrk 231 is a milli-parsec black-hole binary with little intrinsic reddening. The large-mass black hole experiences advection-dominated accretion, emitting little continuum, while the accretion disk of the small-mass black hole emits as an ordinary quasar, dominating the observed weak UV continuum and contributing all of the photoionizing flux. We demonstrate that this model is untenable for four reasons. (1) To produce the observed near-infrared emission lines, the equivalent widths would have to be  $\sim 100$  times larger than typical values with respect to the photoionizing continuum, a situation that seems energetically unlikely. (2) We use the photoionization code *Cloudy* to demonstrate it is not possible to produce the He I\* emission line intensity for the observed He I\*/P $\beta$  flux ratios, even if the line-emitting gas intersects all of the photoionizing light. (3) We also show that while the He I\*/C IV line ratio is sensitive to the spectral energy distribution, the observed ratio is  $\sim 100$  times higher than that of PHL 1811, an intrinsically X-ray weak quasar whose weak C IV line is well explained by its soft spectral energy distribution. (4) The observed continuum provides insufficient energy to power the thermal near- and mid-infrared emission. We find that the He I\*/P $\beta$  ratio is sensitive to the spectral energy distribution for a one-zone model. If this sensitivity is maintained in general broad-line region models, then this ratio may prove a useful diagnostic for heavily reddened quasars.

*Subject headings:* accretion — quasars: emission lines — quasars: individual (Mrk 231) — quasars: supermassive black holes

---

<sup>1</sup>Visiting Astronomer at the Infrared Telescope Facility, which is operated by the University of Hawaii under Coop-

---

erative Agreement no. NNX-08AE38A with the National Aeronautics and Space Administration, Science Mission Di-

## 1. Introduction

The confirmed existence of a milli-parsec-separation supermassive black hole binary (SMBH) binary would be an important discovery. SMBH binaries may be present in nature as a consequence of hierarchical mergers of dark matter halos, so the incidence of binary AGN provides a potentially important test of galaxy assembly models. They may be the strongest sources of gravitational wave emission, and are therefore potentially important probes of general relativity.

Mrk 231 is a well-known, nearby ( $z = 0.0421$ ) ultraluminous infrared galaxy that has a Seyfert 1 optical spectrum (Sanders et al. 1988). The infrared emission is thought to be a combination of AGN and starburst activity (e.g., Farrah et al. 2003, and references therein). Recently, attention has been again drawn to this galaxy after the discovery of a powerful, wide-angle, kiloparsec-scale molecular outflow (Rupke & Veilleux 2011).

Mrk 231 has an unusual UV-through-infrared spectral energy distribution (SED). While the optical through infrared SED appears typical of quasars, the spectrum is strongly cut off through the near UV, and the continuum is very weak toward shorter wavelengths. The near-UV-through-infrared SED was studied by Leighly et al. (2014). We found that the unusual shape was consistent with circumstellar reddening, which is distinguished by a large covering fraction, and large optical depths, approaching one, that produce increased extinction in the blue and UV, with red light scattered back into the line of sight as a secondary effect. This type of reddening has been observed in Type 1a supernovae (Wang 2005; Goobar 2008). Veilleux et al. (2013) also interpreted the unusual near-UV-through-optical spectral energy distribution in terms of reddening, although their proposed reddening mechanism was somewhat different.

Yan et al. (2015) propose an alternative explanation of the unusual SED. They suggest that Mrk 231 hosts a milli-parsec binary black hole system, with nearly negligible reddening. The smaller-mass black hole ( $4.5 \times 10^6 M_{\odot}$ ) accretes as a thin disk and dominates the weak UV emission. The larger-mass black hole ( $1.5 \times 10^8 M_{\odot}$ ) has a low ac-

cretion rate and radiates inefficiently as an Advection Dominated Accretion Flow (ADAF). These two black holes are surrounded by a circumbinary disk, which dominates the optical and IR, and the steep rolloff observed toward the UV is caused by the inner edge of the circumbinary disk. Moreover, they suggest that a steep rolloff from the optical toward the UV is a characteristic signature of binary black holes, and thus finding objects with similar spectra provides a method to discover these objects. A not-to-scale schematic diagram of the model is shown in Fig.1; see also Yan et al. (2015, Figure 1).

In this paper, we critique the binary black hole model for Mrk 231 presented by Yan et al. (2015); in particular, we examine whether the binary black hole model can produce the observed emission lines. In §2, we review the features and assumptions of the Yan et al. (2015) model relevant to the production of the emission lines. §3 motivates our use of near-infrared emission lines, combined with C IV, as diagnostics, and describes the data that we compiled. §4 lays out the several spectral energy distributions used for simulations. §5 reports the results obtained using a set of one-zone *Cloudy* models. §6 summarizes our results: we find that the binary black hole model cannot produce the observed emission lines. We also show that the binary black hole model cannot power the observed mid-infrared continuum (torus) emission. We briefly discuss the potential utility of the infrared emission lines for constraining the intrinsic spectral energy distribution in obscured quasars.

## 2. The Yan et al. (2015) Model

A critical feature of the Yan et al. (2015) model is that only the emission from the small mass black hole contributes significantly to the photoionizing continuum. They identify the continuum of the small-mass black hole with the weak far-UV continuum emission (Veilleux et al. 2013), while the near-UV through infrared emission originates in the circumbinary disk. Thus, their model requires that the photoionizing flux of a small mass black hole power the line emission of a quasar with a combined mass of  $\sim 2$  orders of magnitude larger. The result, as we will show in §3.2, is that the near-infrared lines that we observe would therefore need to have equivalent widths with respect

---

rectorate, Planetary Astronomy Program.

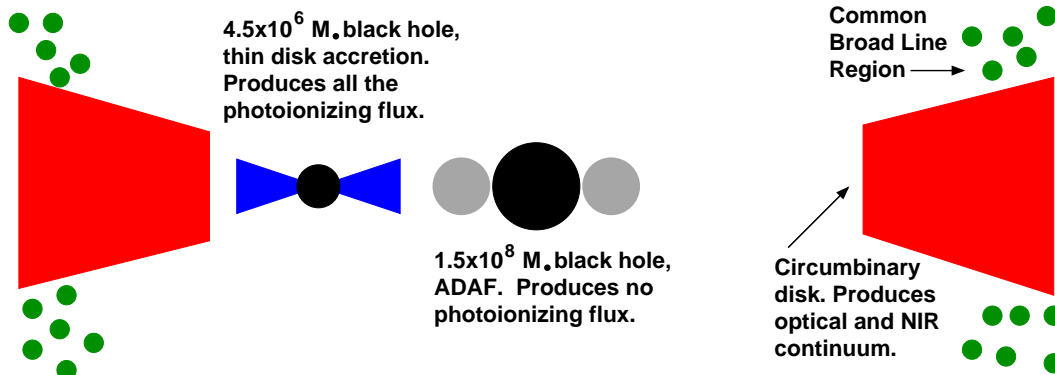


Fig. 1.— A schematic diagram of the Yan et al. (2015) binary black hole model for Mrk 231; see also Yan et al. (2015, Figure 1) for a face-on view. The smaller  $4.5 \times 10^6 M_{\odot}$  black hole accretes as a thin disk and radiates efficiently, thereby emitting all the photoionizing flux that powers the broad-line region emission, while the larger  $1.5 \times 10^8 M_{\odot}$  black hole accretes at a low rate, as an ADAF, and thus radiates inefficiently, producing no significant photoionizing flux. The BLR is predicted to be about 1.5 times the radius of the inner edge of the circumbinary disk, and is required emit at more than 100 times the flux of a typical BLR to produce the observed near-infrared emission lines.

to the photoionizing continuum (rather than the observed continuum) about 100 times larger than normal.

Yan et al. (2015) make assumptions about the spectral energy distribution of the small mass black hole that result in a relatively high fraction of its emission emerging in the far UV. Inferred to be accreting at a significant fraction of Eddington, this accretion disk would be expected to be relatively bright. In addition, since the black hole mass is relatively small for a quasar, the inner-edge temperature would be high. They also assume that the optical-UV continuum is very blue, having the slope of the sum-of-blackbodies accretion disk, i.e.,  $F_{\nu} \propto \nu^{1/3}$ . In contrast, quasars are generally observed to have a redder optical-UV continuum, closer to  $F_{\nu} \propto \nu^{-0.5}$ ; this is one of the unexplained mysteries of accretion disks, along with the lack of polarization and Lyman edges (Koratkar & Blaes 1999). Finally, they assume that the X-ray flux is negligible. This is inconsistent with observations, as we show in §4. These factors combine to make their assumed accretion disk emit a maximally high fraction of its continuum in photoionizing photons. We explore the predicted emission from their optimized spectral energy distribution in §5, along with the predicted emission using more typical SEDs, and show that

none of them can produce the observed flux of the near-infrared helium and hydrogen broad lines.

Yan et al. (2015) also address the question of line emission, in their §6. They make a simple nebular approximation and compute the expected number of  $H\alpha$  photons resulting from recombination of hydrogen in a gas illuminated by their assumed spectral energy distribution. They predict that sufficient  $H\alpha$  emission would be produced if the global covering fraction is  $\Omega \sim 0.5$ . However, this analysis is insufficient, first, because in quasars, the hydrogen lines are produced in the partially-ionized zone, and the line ratios and fluxes are observed to be dramatically different from those predicted in the simple nebular approximation (e.g., Osterbrock & Ferland 2006; Kwan & Krolik 1981). In addition, quasars produce other emission lines besides the Balmer lines, and it is not obvious that those would be produced with sufficient strength to match observations. We perform a more realistic line analysis in §5.

### 3. Data

#### 3.1. Emission Lines Considered

Our goal in this paper was to determine whether the line emission observed in Mrk 231 is consistent with the binary hypothesis put forth

by Yan et al. (2015), not to provide a full model of the emission lines. Therefore we considered just a few lines that provide sufficient diagnostic power.

We focused on the near-infrared spectrum because that region is relatively free of the effects of reddening, regardless of the interpretation of the continuum. The spectrum was observed using the SpeX instrument on the IRTF, and the details of the observation can be found in Leighly et al. (2014). We use He I\* $\lambda$ 10830, a line that arises from recombination of once-ionized helium. The energy required to create He<sup>+</sup> is 24 eV, and therefore He I\* probes the H II part of the broad-line region emission. Being a recombination line, it is principally a diagnostic of the flux of the ionizing continuum on the broad-line-region gas. For example, for a semi-infinite slab, the flux of this line is monotonic with the helium-continuum photoionizing flux.

We also used Paschen  $\beta$  at 12818Å and Paschen  $\alpha$  at 18751Å. Paschen  $\beta$  occurs in close proximity to the He I line in the spectrum, so reddening does not affect their line ratios significantly. The ratio of Paschen  $\alpha$  to Paschen  $\beta$  can be influenced by reddening, but much less than, for example, the Balmer lines, given that reddening curves tend to flatten toward the near infrared.

The Paschen lines are recombination lines of hydrogen, and their fluxes and ratios are influenced strongly by the physical conditions of the line-emitting gas. For example, although these lines are produced throughout the ionized gas slab, a significant amount is produced beyond the hydrogen ionization front, in the partially-ionized zone. In fact, our simulations (§5) show that a significant column of partially-ionized gas is required for these lines to be observable against the bright quasar continuum. In the partially-ionized zone, the opacity to Lyman lines can be very large, and hydrogen line ratios are dramatically different from those predicted in the simple nebular approximation (e.g., Osterbrock & Ferland 2006; Kwan & Krolik 1981). For example, absorbed and thermalized Ly $\alpha$  can create a significant population of hydrogen in  $n = 2$ , which can then suffer photoionization by photons with wavelengths shorter than 3646Å. X-ray photoionization is also important. In addition, while hydrogen in  $n = 1$  cannot be collisionally excited because the difference in energy between  $n = 1$  and  $n = 2$  is too

large, hydrogen in  $n = 2$  can experience collisional excitation, and this process will contribute to the Balmer and Paschen lines. The presence of a population of hydrogen in  $n = 2$  means that Balmer lines will also experience significant optical depths, reducing the radiative de-excitation and cooling. Additional processes such as charge exchange and collisional de-excitation may also contribute. Turbulence or differential velocities will change the line optical depth, further altering the line ratios (e.g., Bottorff et al. 2000). This means that the recombination line fluxes and ratios are best estimated using a photoionization code such as *Cloudy*, which accounts for all of these processes.

We use C IV $\lambda\lambda$ 1548,1551 to probe the UV where reddening will be important. C IV is a collisionally excited line that is produced in the H II portion of the broad-line region. It is generally one of the strongest lines present in quasar spectra, and is an important coolant, a consequence of the relatively high abundance of carbon, and its easy excitability, as C<sup>+3</sup> has only one valence electron.

In this paper, we simply use as our diagnostics the strength of the He I\* line (either the equivalent width of the line, or the predicted flux, depending on the situation; see below), and the line flux ratios He I\*/P $\beta$ , P $\alpha$ /P $\beta$ , and He I\*/C IV. Thus, we are leaving out a great deal of physics known to be relevant to the broad line region. For example, we do not take into account the fact that the BLR is not likely to be characterized by a single set of physical parameters (ionization parameter, density, column density) but rather to be a combination of gas from a range of parameters. This latter case is addressed by the Locally Optimally Emitting Clouds (LOC) models (Baldwin et al. 1995), and LOC models for some of the lines considered in this paper have been investigated by Ruff et al. (2012). In this paper we consider a one-zone photoionization model, principally because it is sufficient to prove our point, as the effect that we see is very apparent, even without photoionization analysis, as described in §3.2.

It is also known that various emission lines can have different shapes that reflect an origin in kinematically different gases. For example, in some relatively rare cases, the high-ionization lines such as C IV can be broad and strongly blueshifted,

while intermediate- and low-ionization lines are narrow and symmetric about the rest wavelength (e.g., Leighly 2004, and references therein). We do not address this in our analysis either, again because the result we find is not subtle, and because the line profiles in Mrk 231 don't warrant this consideration.

Finally, the emission lines are known to respond to the shape of the spectral energy distribution (SED). If the SED is hard, i.e., the X-ray band is strong relative to the UV, then high-ionization lines are observed to be strong (e.g., Casebeer et al. 2006). If the SED is soft, then the high-ionization lines are observed to be weak (Leighly et al. 2007a). We address this effect by considering several spectral energy distributions that span the range of shapes observed, to first approximation.

### 3.2. Mrk 231

The He I\*, P $\beta$ , and P $\alpha$  lines were modeled in Leighly et al. (2014), and we take those measurements from that analysis.

*HST* has observed the C IV region twice, and both observations are available in the archive. The first observation was taken in 1996 with FOS and is shown in Gallagher et al. (2002). The second one was taken in 2014 using COS. They are consistent with one another, although the COS spectrum has much better signal-to-noise ratio. We measure the flux in the C IV line in the COS spectrum by fitting it with two Gaussians.

Analysis of the near-infrared line equivalent widths shows us, in a simple way, why the Yan et al. (2015) model is untenable. Broad line emission is a characteristic property of quasars, and the pattern of the broad line emission (e.g., the lines observed, their equivalent widths, and their ratios) is roughly the same over a factor of  $\sim 10,000$  in inferred black hole masses and luminosities. That is not to say that line emission is identical from one object to the next; there are consistent patterns such as the Baldwin effect, but these account for a variation of less than one order of magnitude in equivalent width over four orders of magnitude in luminosity (e.g., Dietrich et al. 2002, Fig. 7). The constancy of the line equivalent widths means that photoionizing flux that powers the emission lines scales with the contin-

uum under the emission lines. Thus, luminous quasars have luminous BLR emission, and less luminous AGN have less luminous BLR emission. So it is not reasonable to expect that a small black hole will be able to power the line emission of a luminous quasar.

This idea is investigated qualitatively in Fig. 2, which shows a variation of Leighly et al. (2014) Figure 5, where instead of focusing on the continuum only, we also examined the emission lines. We first overlaid the intrinsic continuum, inferred in Leighly et al. (2014), based on the Richards et al. (2006) composite continuum spectrum, with an optical-IR composite created by joining the SDSS composite (Vanden Berk et al. 2001) to the SDSS/IRTF composite (Glikman et al. 2006) at around 4000Å. The merged composite provides infrared coverage, and avoids the well-known long-wavelength flattening present in the SDSS quasar composite due to significant host galaxy contributions seen in the lower luminosity quasars that dominate the SDSS composite on the red end of the visible band. The match is good except at very long wavelengths where an additional hot blackbody component contributes to the emission in Mrk 231 (Leighly et al. 2014).

Next, we applied the Goobar (2008) reddening curve, using the parameters that we inferred in Leighly et al. (2014), to the quasar composite spectrum. Overlaid upon that is the observed Mrk 231 spectrum. It can be seen that the overall agreement is very good through the optical and near UV where the line emission is relatively typical of quasars. Mrk 231 has somewhat stronger Fe II emission, and somewhat weaker Balmer emission, but the difference is within the range observed among AGN and quasars. Moreover, the reddened composite spectrum also provides a reasonable match to the near-UV continuum, against which the Mg II and Fe II broad absorption lines expected in this FeLoBAL can be seen. We discuss the discrepancy in the far-UV in §6.6.

According to the Yan et al. (2015) model, the continuum from the normally-accreting small black hole is swamped by the circumbinary disk emission through the optical and infrared, but it becomes visible in the UV, shortward of the rolloff caused by the inner edge of the circumbinary disk. The gray dashed line in Fig. 2 shows the Richards et al. (2006) continuum scaled to

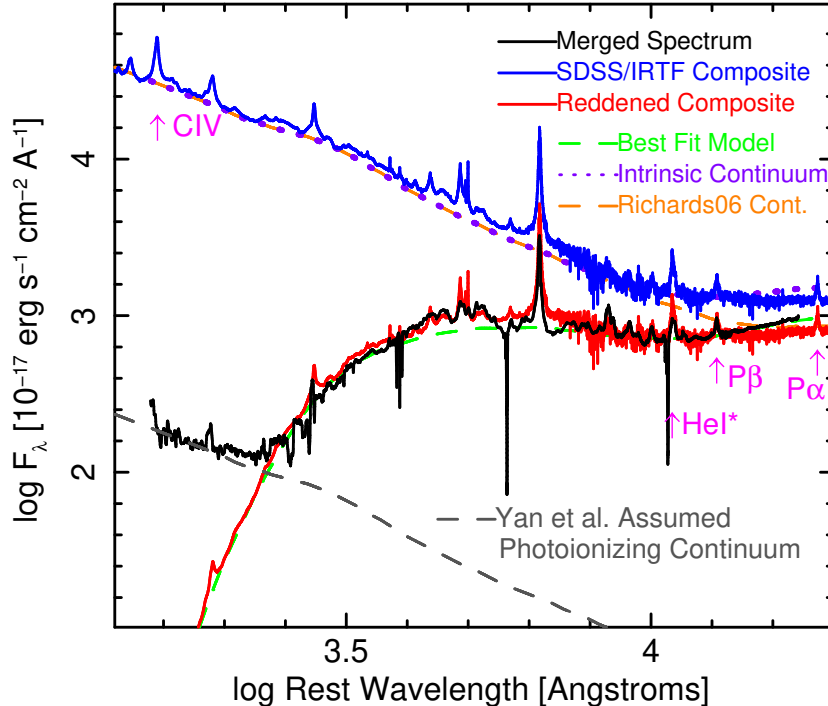


Fig. 2.— Adapted from Leighly et al. (2014) Figure 5. We show the observed broad-band spectrum from Mrk 231 (black) overlaying the best-fitting continuum model (dashed green) developed using the Richards et al. (2006) continuum (dashed orange) plus a blackbody component from hot dust (dotted purple), and subject to the circumstellar reddening; see Leighly et al. (2014) for details. Overlaid is a composite spectrum created merging the SDSS quasar composite (Vanden Berk et al. 2001) and the IRTF quasar composite (Glikman et al. 2006) in solid blue, and subject to the same reddening, in solid red; see Section 3.2 for details. This yields a good fit over most of the bandpass, except for the continuum shortward of  $\sim 2200\text{\AA}$ ; this is a separate component that may arise from scattering (§6.6). We also overlay the Richards et al. (2006) continuum scaled to match the continuum flux at  $2000\text{\AA}$  (dashed gray). In the Yan et al. (2015) model, this taken to be the emission from the accretion disk of the small-mass black hole. The wavelengths of the four diagnostic lines used in this paper are marked.

match the near-UV spectrum; this represents the putative continuum of the small black hole. In the region of the infrared lines of interest, around 1 micron, this continuum is a factor of  $\sim 100$  below the observed Mrk 231 continuum. *Thus, if the small black hole is producing all of the photoionizing photons in the system, then the infrared line equivalent widths would have to be a factor of  $\sim 100$  larger than typical with respect to the small black hole continuum in order to show the observed equivalent widths with respect to the observed continuum.* This does not seem reasonable, as such huge equivalent widths have never been seen. In-

deed, as we will show in §5.2, the smaller black hole continuum lacks sufficient power to produce the observed infrared line emission.

We used the inferred luminosities to estimate the radius of the broad line region. Interpolating the flux density at  $5100\text{\AA}$  from the Leighly et al. (2014) intrinsic continuum and the Yan et al. (2015) photoionizing continuum (orange and gray lines in Fig. 2), and using the “clean” parameters for the radius/luminosity relationship from Bentz et al. (2013), the  $H\beta$  emitting BLR is estimated to be located 99 and 6.5 light days from the central engine for the reddened and the binary

black hole interpretations, respectively. The first value seems typical for a quasar, while the second value is small among reverberation-mapped AGN (Bentz et al. 2013). Relatively rapid variability of  $H\beta$  would be predicted; that has never been reported. Moreover, the radius of the inner edge of the circumbinary disk is estimated by Yan et al. (2015) to be 4.2 light days from the center. So, in the Yan et al. (2015) scenario, the BLR would have to be located on top of the circumbinary disk, close to its inner edge, and, as discussed above, would have to emit more than 100 times the normal flux of a typical broad-line region.

### 3.3. Comparison Sample

In order to interpret the line emission from Mrk 231, we looked at the characteristic properties of other active galaxies. A sample of infrared spectra of nearby Seyfert galaxies and quasars was presented by Landt et al. (2008), and we took He I\*,  $P\beta$ , and  $P\alpha$  (when available) line fluxes from this reference. We excluded Mrk 590 because it has turned into a Seyfert 2 (Denney et al. 2014). We also excluded NGC 3227 as it is highly reddened (Crenshaw et al. 2001). This leaves 15 objects with measurements for these three lines and C IV from the literature (see below), and three more objects with measurements for only He I\*,  $P\beta$ , and C IV. Among these 18 objects, 14 have black hole masses<sup>2</sup>. The range of log black hole masses represented, in units of solar mass, is 6.88 to 8.84, with a mean of 7.66 and standard deviation of 0.54. The range therefore is a bit higher than the log black hole mass inferred for the small mass black hole (6.65 [solar masses]). However, we found that two objects with small log black hole masses, NGC 4051 (6.130) and NGC 4748 (6.41), have infrared line properties (Riffel et al. 2006) consistent with the range of our comparison sample.

Landt et al. (2008) attempted to deconvolve the emission lines in terms of a broad line and a narrow line. This is an uncertain procedure unless there is a break in slope between the broad and narrow line (i.e., as in a Seyfert 1.5 or 1.8); in general, it is difficult to determine how much of the line should be ascribed to the narrow line region, especially when the line is cuspy. To avoid this uncertainty, we used the total line flux, i.e.,

the sum of the narrow and broad line fluxes in Landt et al. (2008) Table 5. We note that the narrow line flux is generally much smaller than the broad line flux (the median ratio of narrow to broad line flux is about 9%), so this approximation does not increase the uncertainty significantly. Moreover, we used the line ratios of the comparison sample simply as an indication of the range of ratios observed in nature, so high precision is not required.

Reddening influences the He I\*/ $P\beta$  ratio minimally for typical objects; for example, a modest  $E(B - V) = 0.1$  and an SMC reddening curve results in a decrease in this ratio by about 2.3%. The difference is larger for a heavily-reddened object like Mrk 231, where the Goobar (2008) reddening curve with the parameters measured by Leighly et al. (2014) yield a decrease in the ratio of 8.3%. It is somewhat more important for the  $P\alpha/P\beta$ , where  $E(B - V) = 0.1$  increases the ratio by 3.4% (19% for the reddening measured in Leighly et al. (2014)). The influence of reddening can be quite strong for He I\*/C IV: that ratio is a factor of 2.9 for  $E(B - V) = 0.1$ . However, we think that at least some of the large range of He I\*/ $P\beta$  ratios is intrinsic, rather than a consequence of reddening, because the dispersion, parameterized by the standard deviation divided by the mean, is similar for the He I\*/ $P\beta$  ratio (0.37) and the He I/C IV ratio (0.81). If reddening were dominating the range of observed He I\*/ $P\beta$  ratios, then a much larger dispersion would be expected for the He I/C IV ratio.

As an extreme case, we also included data from the intrinsically X-ray weak quasar PHL 1811 (Leighly et al. 2001, 2007a,b). We analyzed a spectrum from our observations made using IRTF SpeX on 2008 August 22, 23, and 24. We fit the continuum with a polynomial, and the emission lines with Lorentzian profiles in the region of the spectrum including He I\* and  $P\beta$ , requiring that the Paschen lines (i.e., the isolated  $P\beta$  line and the blended  $P\gamma$  line) have the same width and separation based on rest wavelengths. Several Fe II lines were modeled with Gaussians. We model the self-absorption on the He I\* emission line using a Gaussian optical depth profile.  $P\alpha$  is relatively isolated and is well modeled with a Lorentzian profile.

We turned to the literature for C IV mea-

<sup>2</sup><http://www.astro.gsu.edu/AGNmass/>

measurements. Some objects in the Landt et al. (2008) sample did not have any UV spectroscopic observations; these include IRAS 1750+508, H1934–063, and H 2106–099, and thus they were dropped from the sample. We extracted as many measurements as possible from Kuraszekiewicz et al. (2002), Kuraszekiewicz et al. (2004), and/or Tilton & Shull (2013) because they presented a uniform analysis of large sets of *HST* spectra. Other sources of *HST* measurements included O’Brien et al. (2005) for PDS 456, Laor et al. (1994) for 3C 273 and H1821+643, Kriss et al. (2000) for NGC 7469, and Leighly et al. (2007b) for PHL 1811. There were only *IUE* measurements available for Mrk 79, PG 0844+349, Mrk 110 and NGC 4593, compiled in Wang et al. (1998). These were used with caution because comparison of values from the subset of objects that also had observations using *HST* showed that the Wang et al. (1998) measurements were consistently a factor of  $\sim 10$  lower. We suspected that the flux-units footnote on Wang et al. (1998) Table 1 is too low by a factor of 10, and we therefore multiplied their values by 10.

The UV spectroscopic observations were not made simultaneously with the infrared spectroscopic observations, so relative variability is a concern. We estimated the importance of this effect by compiling C IV measurements from multiple *HST* observations when available; objects with multiple measurements have both blue and green points for their He I\*/C IV ratio in Fig. 3. Examination of this figure shows that the He I\*/C IV ratio varies more across the sample than it does for any single object (quantified below), and therefore relative variability is not important. Again, our intention was to estimate the range of the He I\*/C IV ratio observed in nature, and high precision is not necessary.

### 3.4. Observed Ranges of Line Properties

In order to interpret the line ratios from Mrk 231, we derived the range of line properties observed in the comparison sample. These ranges are used to constrain the simulations discussed in §5. Fig. 3 shows the ratios He I\*/P $\beta$ , P $\alpha$ /P $\beta$ , and He I\*/C IV as a function of luminosity in the He I\* line.

Consider first the He I\*/P $\beta$  ratio, shown in the top left panel. This ratio lies between 0.37 and 2.52 (a range of a factor of  $\sim 7$ ), with mean and

standard deviation of  $1.67 \pm 0.61$ . For Mrk 231, we show the observed ratio, and the ratio after correcting for the reddening inferred in Leighly et al. (2014). Neither Mrk 231 nor PHL 1811 have exceptional values of this ratio. To constrain the simulations, we use an upper limit of 2.5 (as observed) but extend the lower limit to 0.1 in order to roughly compensate for possible contribution of He I\* emission from an outflowing component.

The P $\alpha$ /P $\beta$  ratio is shown in the middle panel. This ratio lies between 0.94 and 1.74 (a factor of 1.84), with mean and standard deviation of  $1.20 \pm 0.21$  for the comparison objects. The observed ratio for Mrk 231 is slightly high compared with this range (1.79); however, when corrected for the reddening curve inferred by Leighly et al. (2014), the ratio drops to 1.58, a value roughly consistent with that of the comparison sample. To constrain the simulations, we consider values between 0.9 and 2.0.

The observed ratios of P $\alpha$ /P $\beta$  indicate high optical depths. As discussed in Osterbrock & Ferland (2006), in the low-density, low-optical-depth limit (Case A), and the large-optical-depth limit whereby every Lyman-line photon is scattered many times (Case B) predict P $\alpha$ /P $\beta$  ratios of 2.33 and 2.28 respectively. Our ratios are lower than that, suggesting significant optical depth in higher order Paschen lines.

The range of observed He I\*/C IV ratios is large in the comparison sample (0.025 to 0.37, a factor of  $\sim 15$ ), with a mean of 0.11 and a standard deviation of 0.089. PHL 1811 has a rather large ratio of  $\sim 0.3$ . The values for Mrk 231 are very large: 31.5 as observed, and 10.8 corrected for  $E(B-V) = 0.1$  using an SMC reddening curve (see § 4). We note that it is not possible to correct C IV from Mrk 231 using the Goobar (2008) reddening curve; as can be seen in Fig. 2, the reddening is completely optically thick at those wavelengths, and the observed continuum and lines has a different origin, perhaps in scattered light (§6.6). For the simulations, we set a lower limit of 0.025 on the He I\*/C IV ratio, but do not set an upper limit in order to see if we can attain the high values observed from Mrk 231.

## 4. Spectral Energy Distributions

As discussed above, Yan et al. (2015) assumed a spectral energy distribution that maximally fa-



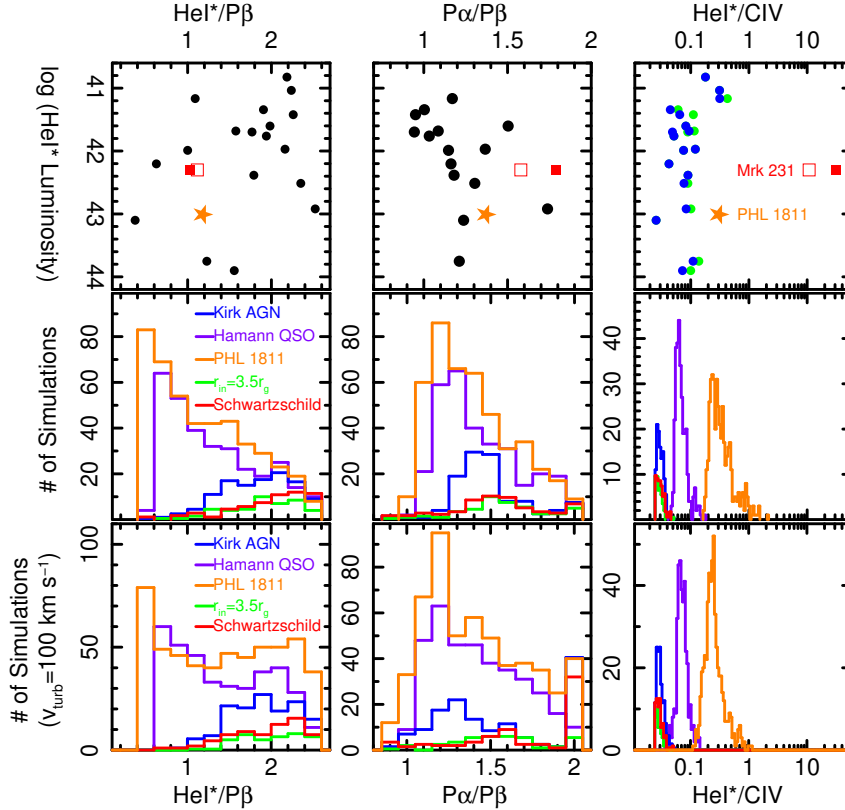


Fig. 3.— **Top Panels:** Observed He I\*/Pβ, Pα/Pβ, and He I\*/C IV ratios from Mrk 231 (filled red squares), the intrinsically X-ray weak quasar PHL 1811 (orange star), and a comparison sample taken from Landt et al. (2008) (filled circles). Also shown are ratios for Mrk 231 corrected using the reddening curve inferred by Leighly et al. (2014) (for infrared ratios He I\*/Pβ and Pα/Pβ) and using an SMC reddening curve with  $E(B - V) = 0.1$  for the He I\*/C IV ratio (open red squares). Mrk 231 and PHL 1811 have typical infrared line ratios, while PHL 1811 has a somewhat high He I\*/C IV ratio, due to its weak high-ionization line emission (Leighly et al. 2007b). The He I\*/C IV ratio for Mrk 231 is much higher (note the logarithmic axis), due to the low C IV flux. It is likely that we do not observed the intrinsic C IV emission from Mrk 231. **Middle Panels:** The distributions of results from *Cloudy* simulations selected to be consistent with the adopted ranges of He I\*/Pβ and Pα/Pβ ratios, the lower limit of He I\*/C IV, and observed values of either He I\* flux or equivalent width. These panels show that the *Cloudy* models are able to match the observed ranges of the comparison sample ratios, and the He I\*/Pβ suggests diagnostically useful SED dependence, along with He I\*/C IV, assuming appropriate reddening corrections can be made. **Bottom Panels:** The same as the middle panels, but including a turbulent velocity in the simulations. The results are not substantially different from the static case.

vors their interpretation. In this section, we reconstruct their SED, correcting for the observed X-ray emission, and compare it with more typical spectral energy distributions that roughly span the range observed from AGN and quasars, along with the extreme X-ray weak SED observed from

PHL 1811. The properties of the spectral energy distributions are listed in Table 1.

We first considered two spectral energy distributions previously used to model lines from AGN and quasars. A relatively hard one was adopted

from Korista et al. (1997)<sup>3</sup>, and a relatively soft one that may be more typical of quasars taken from Hamann et al. (2011)<sup>4</sup>. These spectral energy distributions are shown in Fig. 4, arbitrarily normalized to intersect the near-UV portion of the SMC- $E(B - V) = 0.1$ -corrected Mrk 231 spectrum.

We then reconstructed the Yan et al. (2015) SEDs. First, Yan et al. (2015) infer a small amount of intrinsic reddening, between  $E(B - V) = 0.07$  and  $E(B - V) = 0.14$ , depending on the model, for an SMC reddening curve (Pei 1992). Therefore, we required the spectral energy distributions discussed in this section to intersect the near UV emission observed from Mrk 231 at 2000Å, either as observed, or dereddened by an intermediate value,  $E(B - V) = 0.1$ .

Teng et al. (2014) presented an analysis of *Chandra* and *NuSTAR* observations of Mrk 231. They found an absorbed, weak hard X-ray continuum with a flat ( $\Gamma \sim 1.4$ ) photon index that they take to be the intrinsic X-ray continuum of the quasar. Yan et al. (2015) did not consider the X-ray emission in their paper. They felt that they were justified in this assumption because Teng et al. (2014) noted that Mrk 231 is X-ray weak ( $\alpha_{ox} \sim -1.7$ ).<sup>5</sup> However, Teng et al. (2014) inferred that the observed UV is absorbed, and estimated  $\alpha_{ox}$  based their estimate of the *intrinsic* optical/infrared spectrum (Veilleux et al. 2013, Figure 3), not the observed one. With respect to the observed UV continuum, Mrk 231 is rather X-ray bright.

The deconvolved X-ray spectrum is shown in Figure 5 of Teng et al. (2014). We digitized the “Direct PL” component of that plot between 8.4 and 19.9 keV. We needed to multiply the result by a factor of 1.29 in order to match the 0.5–30 keV luminosity in their Table 1 for the MyTorus model. The Teng et al. (2014) power law is shown in dark gray in Fig. 4. We required that the reconstructed Yan et al. (2015) spectral energy dis-

tributions intersect this X-ray data, and having a spectrum  $F_\nu \propto \nu^{-0.28}$  (the slope we measure from the digitized spectrum), breaking to a slope of  $-2$  for energies higher than 25 keV, the limit of the *NuSTAR* spectrum.

Yan et al. (2015) assumed, for the disk around the smaller-mass black hole, an inner radius  $r_{in} = 3.5r_g$  in order to produce a radiative efficiency of  $\eta = 0.1$ . Then, their best-fitting model yielded a value of the smaller black hole mass of  $4.5 \times 10^6 M_\odot$  radiating at  $0.6L_{Edd}$ . They assumed that the optical-UV spectrum of the smaller black hole is characterized by a sum-of-blackbodies accretion disk model (e.g., Frank et al. 2002). The outer edge of the disk was taken to be 100 times the inner edge. This information was sufficient for us to follow Yan et al. (2015) and compute a disk spectrum from the infrared through the far UV (i.e., through the high-temperature rolloff). The disk spectrum was then normalized to the observed 2000Å flux, and the X-ray spectrum as described above joined to the infrared-through-UV spectrum. This SED is shown in Fig. 4, and information about this continuum is given in Table 1.

When we normalized the  $r_{in} = 3.5r_g$  spectrum to the Mrk 231 continuum corrected for  $E(B - V) = 0.1$  at 2000Å, we found that the emission is super-Eddington ( $L/L_{Edd} = 1.14$ ). Yan et al. (2015) found it to be sub-Eddington, possibly because they did not include the X-ray emission. So, we normalized the  $r_{in} = 3.5r_g$  SED to the observed Mrk 231 continuum at 2000Å, rather than the  $E(B - V)$  dereddened one. But in order to give the Yan et al. (2015) model the best chance for success (i.e., the highest possible photoionizing flux), we also considered a Schwarzschild disk, i.e.,  $r_{in} = 6r_s$ , normalized to the Mrk 231 spectrum corrected for intrinsic absorption of  $E(B - V) = 0.1$ ; it is also shown in Fig. 4. This SED is not super-Eddington (Table 1).

These two spectral energy distributions have relatively flat values of  $\alpha_{ox}$  of  $-1.28$ , when normalized to the observed continuum, and  $-1.45$  when normalized to the  $E(B - V) = 0.1$  dereddened one.  $\alpha_{ox}$  is related to the UV monochromatic luminosity at 2500Å (e.g., Steffen et al. 2006); those regression relationships predict  $\alpha_{ox}$  to be  $\sim -1.6$ . This is somewhat steeper than inferred,

<sup>3</sup>This SED is taken as a typical AGN spectral energy distribution and is called by the *Cloudy* command `AGN kirk`, or, equivalently `AGN 6.00 -1.40 -0.50 -1.0`.

<sup>4</sup>This SED is called by the *Cloudy* command `AGN T=200000K, a(ox)=-1.7, a(uv)=-0.5, a(x)=-0.9`.

<sup>5</sup> $\alpha_{ox}$  is the point-to-point slope between the ultraviolet continuum measured at 2500Å and the X-ray continuum measured at 2 keV.

TABLE 1  
PROPERTIES OF SPECTRAL ENERGY DISTRIBUTIONS

Property	Comparison Sample		Yan et al. 2015		Possible Intrinsic
	Kirk AGN	Hamann QSO	$r_{in} = 3.5r_g$	Schwarzschild	PHL 1811
Reference	Korista et al. (1997)	Hamann et al. (2011)	Yan et al. (2015)+Teng et al. (2014)		Leighly et al. (2007a)
log Bolometric [ $\text{erg s}^{-1}$ ]	N/A	N/A	44.34 <sup>a</sup>	44.50 <sup>b</sup>	45.70 <sup>c</sup>
$L/L_{edd}$	N/A	N/A	0.39 <sup>d</sup>	0.56 <sup>d</sup>	0.17 <sup>e</sup>
$\alpha_{ox}$	-1.40	-1.70	-1.28	-1.42	-2.26
Log Q [ $\text{photons s}^{-1}$ ]	N/A	N/A	54.36	54.61	55.61

<sup>a</sup>SED normalized to observed Mrk 231 continuum at 2000Å. See Fig. 4 and text for details.

<sup>b</sup>SED normalized to Mrk 231 continuum corrected for  $E(B - V)$  at 2000Å. See Fig. 4 and text for details.

<sup>c</sup>SED normalized to Leighly et al. (2014) inferred intrinsic Mrk 231 continuum at 2000Å. See Fig. 4 and text for details.

<sup>d</sup>Calculated using black hole mass  $4.5 \times 10^6 M_{\odot}$  (Yan et al. 2015).

<sup>e</sup>Calculated using black hole mass  $2.3 \times 10^8 M_{\odot}$  (Leighly et al. 2014).

but roughly within the regression uncertainty of 0.24 (Steffen et al. 2006, Equation 2). Since, according to the Yan et al. (2015) model, the bulk of the X-ray emission emerges from the central engine of the small-mass black hole, that system should be relatively X-ray bright, like a Seyfert nucleus.

Fig. 2 and Fig. 4 display the intrinsic continuum inferred using the circumstellar reddening model (Leighly et al. 2014). Interestingly, when we computed  $\alpha_{ox}$  using our inferred intrinsic continuum, and the extrapolation of the Teng et al. (2014) power law, we obtained a value of  $\alpha_{ox}$  of -2.2, essentially the same value observed from the intrinsically X-ray weak quasar PHL 1811 (between -2.2 and -2.4, accounting for X-ray variability, Leighly et al. 2007a). Intrigued by this result, we also investigated whether the extreme X-ray weak PHL 1811 continuum could produce the emission lines observed in Mrk 231 (§5.3).

## 5. Cloudy Models

We used the photoionization code *Cloudy* (Ferland et al. 2013) to see if we could produce the He I\*, P $\beta$ , P $\alpha$ , and C IV lines in the range of strengths and ratios observed. We performed a set of simulations for each of the five continua described in §4. In each case, we perform 5000 or 10,000 simulations with parameters randomly drawn from uniform distributions of ionization parameter ( $-3 \leq \log(U) \leq 1.0$ ), density ( $6 \leq \log(n) \leq 11.5$ ), and a combination parame-

ter defined as the difference between the log of the column density  $N_H$  and the log of the ionization parameter,  $\log(N_H) - \log(U)$ , that measures the thickness of the gas slab relative to the hydrogen ionization front ( $22.5 \leq \log(N_H) - \log(U) \leq 24.0$ ), and has been shown to be useful in analysis of both emission lines and absorption lines (Leighly 2004; Casebeer et al. 2006; Leighly et al. 2007b, 2009, 2011, 2014; Lucy et al. 2014). As discussed below, we performed the entire set of simulations for a stationary gas, and for a gas with a turbulent velocity  $v_{turb} = 100 \text{ km s}^{-1}$ . In all, 80,000 simulations were performed.

We needed a parameter to characterize the strength of the He I\* line. We used the line flux or the line equivalent width, depending on the circumstance. For the Yan et al. (2015) models, it makes most sense to use the observed flux of the line, since, as discussed in §3.2, huge equivalent widths with respect to the photoionizing continuum are required. On the other hand, for the comparison objects, the most convenient parameter is the line equivalent width, although comparison of theoretical and observed equivalent widths can be difficult for infrared lines. For example, the *Cloudy* line fluxes assume full coverage, yet it is known that the broad line region does not fully cover the continuum (or we would always see absorbed continuum spectra in the X-ray band). Leighly (2004) found a covering fraction of 0.05 for intermediate- and low-ionization lines for two rather weak-lined quasars, and we used that value for the lower limit. For the upper limit, we chose

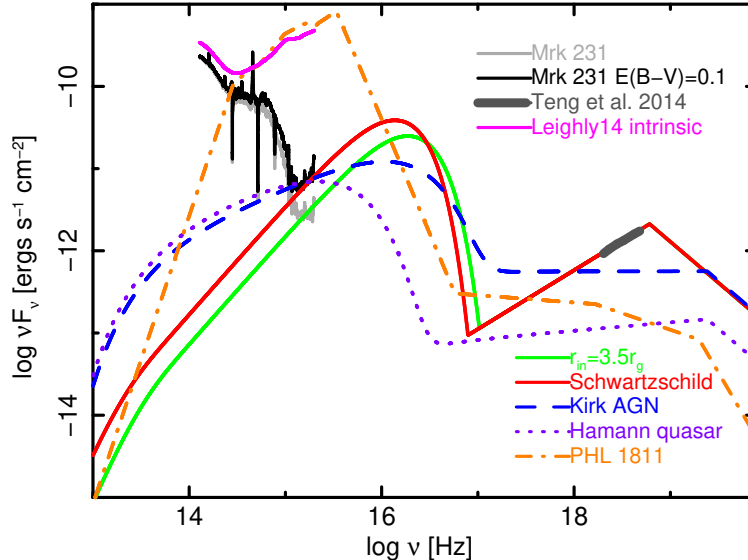


Fig. 4.— Continua used for *Cloudy* simulations, overlaid on the merged Mrk 231 near-UV-to-near-IR merged spectrum from Leighly et al. (2014), and the X-ray results from Teng et al. (2014). Representative “Kirk AGN” and “Hamann quasar” SEDs were used to demonstrate that the *Cloudy* simulations can produce observed He I\* equivalent widths, and He I\*/P $\beta$ , P $\alpha$ /P $\beta$ , and He I\*/C IV ratios in the comparison sample (§5.1). The “ $r_{in} = 3.5r_g$ ” and “Schwartzschild” continua were used to simulate the Yan et al. (2015) model (§5.2). Finally, the “PHL 1811” continuum was used to investigate the line fluxes and ratios for an X-ray weak continuum (§5.3).

a value of 0.5.

Another complication is the observed continuum. The equivalent width from simulations will be with respect to the AGN continuum, while the observations may include a torus component in the near infrared, and/or host galaxy. The comparison sample is dominated by nearby AGN and quasars, and it is likely that the spectroscopic slit excluded much of the galaxy contribution. The He I\* line, at 10830Å, occurs just at the 1-micron break, where the accretion disk continuum and the torus contribution are approximately equal, and so it is expected that the torus contribution will not dominate.

A final complication is that the near infrared portion of the continuum, near 1 micron, lies far from the hydrogen continuum shortward of 911Å, which sets the level of the photoionizing flux. For example, the two SEDs used in §5.1 have optical-UV spectra with  $F_\nu \propto \nu^{-0.5}$ , rather typical of quasars and AGN (e.g., Natali et al. 1998). But

the intrinsic slope is not uniform among AGN, and the larger the difference from  $\nu^{-0.5}$ , the larger the incurred uncertainty in the equivalent width in the infrared band.

We addressed these concerns by considering a rather large range of equivalent width for He I\*. The observed equivalent width range in the comparison sample is 30–300Å, and therefore we accept simulations producing equivalent widths for full covering between 60Å (i.e., lower limit on equivalent width divided by upper limit on covering fraction) and 6000Å (i.e., upper limit on equivalent width divided by lower limit on covering fraction).

Generally speaking, we chose very generous bounds on every parameter in order to give the Yan et al. (2015) model the best chance of proving successful. Therefore, when we show it is not feasible, our result cannot be attributed to an artificial or arbitrary limitation to the considered range of parameter space.

### 5.1. Cloudy Models of the Comparison Sample

We first needed to establish that *Cloudy* can explain the observed He I\* intensity and the observed line ratios from typical AGN and quasars in order to be confident that we could use the *Cloudy* results to analyze special cases. We consider the results from the simulations using the Korista et al. (1997) and Hamann et al. (2011) to bracket the plausible range of SEDs. We extracted the predicted He I\*, P $\beta$ , P $\alpha$ , and C IV fluxes from the simulation results using these two SEDs, and compute the He I\*/P $\beta$ , P $\alpha$ /P $\beta$ , and He I\*/C IV ratios.

We accepted solutions that are consistent with the line ratios in the ranges discussed in §3.4: He I\*/P $\beta$  between 0.1 and 2.5, P $\alpha$ /P $\beta$  between 0.9 and 2.0, and He I\*/C IV larger than 0.025. For the He I\* flux constraint, we used the equivalent width range (for full covering) between 60 and 6000Å, as discussed in §5.

We show the histograms of results from accepted simulations in the lower panels of Fig. 3. Interestingly, SED dependence is present in all the ratios, to a greater or lesser degree. The soft continuum leans towards smaller values of He I\*/P $\beta$ , while the hard continuum produces a larger value of this ratio. This is likely due to the larger contribution in the helium continuum in the hard SED. Both spectral energy distributions tend to favor an intermediate value of P $\alpha$ /P $\beta$ , interestingly close to the mean value observed. This ratio depends principally on optical depth, so a great deal of SED dependence is not expected.

The greatest difference between these two SEDs is in the He I\*/C IV ratio. The hard SED produces only low values of this ratio; that is, it tends to produce relatively large C IV fluxes. This is expected; a harder SED will produce a hotter photoionized gas (e.g., Leighly et al. 2007b, Fig. 14), and C IV is an important coolant, so the proportion of C IV compared with a recombination line like He I\* can be expected to be large when the SED is hard. The softer SED, on the other hand, matches the observed distribution of He I\*/C IV ratios rather nicely.

Fig. 5 shows histograms of the *Cloudy* input parameters for the accepted simulations. The softer SED tends to favor a higher ionization parameter

than the harder one. This is expected; a higher photon flux is necessary for a soft SED to produce the required He I\* flux.

There is a strong localization in densities favored. Investigation of the simulation results showed that this is a consequence of the opacity in the Paschen lines. For fixed  $\log U$  and  $\log N_H - \log U$ , simulations showed that both P $\alpha$  and P $\beta$  became thermalized at larger densities (i.e., the increase of line flux with density broke to a flatter slope), but with P $\alpha$  becoming thermalized at slightly lower densities than P $\beta$ , resulting in a decrease in the P $\alpha$ /P $\beta$  ratio to less than the observed upper limit of  $\sim 2$  near  $\log n_e = 7.5$ , and thus providing a constraint on the density on the low end. At the same time, P $\beta$  became thermalized much faster than He I\*, resulting in a ratio higher than the observed upper limit for the He I\*/P $\beta$  ratio of  $\sim 2.5$  for values greater than  $\log n_e = 9.5$  and thus constraining the density on the high end.

To further investigate the influence of optical depth, we ran the whole set of simulations (i.e., for all SEDs and input parameter ranges), including a turbulent velocity  $v_{turb} = 100 \text{ km s}^{-1}$ . The effect of turbulence is to decrease optical depths (e.g., Bottorff et al. 2000). The chosen value of  $v_{turb}$  is much larger than the thermal line width in a photoionized gas (about  $15 \text{ km s}^{-1}$ ). Physically, it may represent actual macro-turbulence, or differential velocity. This value was chosen arbitrarily because it was large enough to show an effect (no significant effect was observed for  $v_{turb} = 15 \text{ km s}^{-1}$ ). A single value allowed us to understand the effect of turbulence qualitatively. We found that the principal effect of turbulence was a shift of the favored range of density. Investigation of the simulation results showed that, as expected, the opacity is lower in the turbulent case, and thermalization becomes important at higher densities than in the stationary case.

There were a greater number of simulations accepted for larger values of  $\log(N_H) - \log(U)$ , i.e., column density. This is expected by the reasoning discussed above: the Paschen lines are produced predominantly in the partially ionized zone, located beyond the hydrogen ionization front, i.e.,  $\log(N_H) - \log(U) \gtrsim 23.2$ .

These simulations show that these typical AGN and quasar spectral energy distributions are able

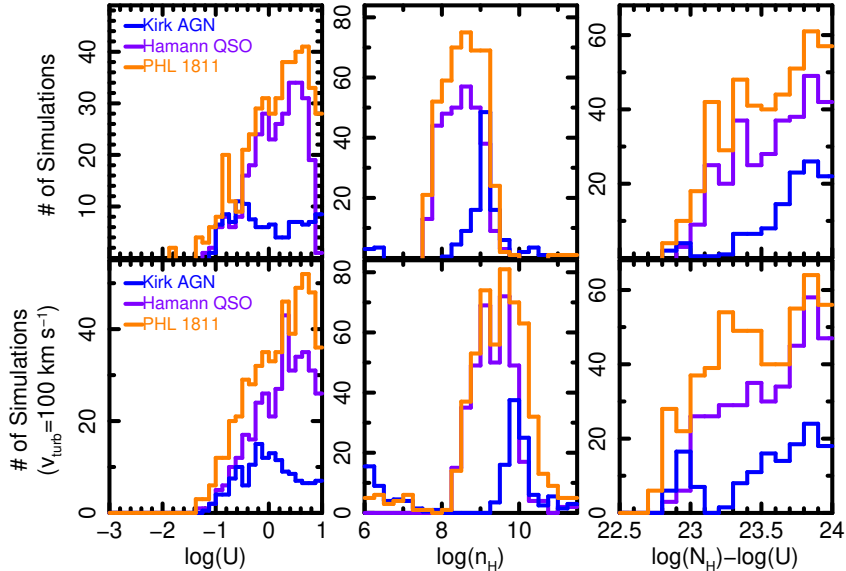


Fig. 5.— The distributions of input parameters from *Cloudy* simulations in which the results were selected to be consistent with the observed ranges of  $\text{He I}^*/P\beta$  and  $P\alpha/P\beta$  ratios, and the lower limit of  $\text{He I}^*/\text{C IV}$  ratios in the comparison sample, and either  $\text{He I}^*$  flux or equivalent width; see text for details. We found that the simulations are consistent with a rather high ionization parameter (higher for softer SEDs, as expected, to meet the requirement of a sufficiently strong helium continuum to yield the observed  $\text{He I}^*$  emission), an intermediate range of density, and a relatively high column density, i.e.,  $\log(N_H) - \log(U) \gtrsim 23$ . The top panels show the results for the stationary case, and the bottom panels show the results for  $v_{\text{turb}} = 100 \text{ km s}^{-1}$ . The principal difference is the favored density range, which is shifted to higher densities for the turbulent case because of reduced thermalization of the Paschen lines as a consequence of lower opacity.

to produce the  $\text{He I}^*$  equivalent widths, and  $\text{He I}^*/P\beta$ ,  $P\alpha/P\beta$ , and  $\text{He I}^*/\text{C IV}$  ratios observed from the typical objects in the comparison sample. We now turn to more specialized cases for comparison.

## 5.2. Cloudy Models using the Yan et al. (2015) Spectral Energy Distributions

*Cloudy* models employing the  $r_{\text{in}} = 3.5r_g$  and the Schwarzschild spectral energy distributions were used to evaluate the viability of the Yan et al. (2015) model. We first asked a basic question: can these SEDs, normalized as described to the observed UV and X-ray emission, produce the  $\text{He I}^*$  flux observed, given the range of observed  $\text{He I}^*/P\beta$  ratios? The advantage of this minimal set of constraints is that it uses only infrared spectral data, and lines that are close to one another, and so will be minimally impacted by red-

dening regardless of model. *We found that neither of these two SEDs could produce the observed  $\text{He I}^*$  flux when constrained to produce the observed range  $\text{He I}^*/P\beta$  ratios, even for a covering fraction of the broad line region equal to 1.* This result is not unexpected given the discussion in § 3.2, i.e., that the near-IR equivalent widths would have to be  $\sim 100$  larger than normal with respect to the photoionizing continuum in order to explain the typical near-infrared line emission observed. It is simply not reasonable to expect the continuum from a  $4.5 \times 10^6 M_\odot$  black hole to be able to power the broad line region emission of a  $> 10^8 M_\odot$  quasar.

While this analysis demonstrates that the Yan et al. (2015) model is not viable, we were also interested in whether these SEDs could possibly explain the unusually large  $\text{He I}^*/\text{C IV}$  ratio inferred. We proceeded as before, working with

the He I\* equivalent width, and the He I\*/P $\beta$ , P $\alpha$ /P $\beta$ , and He I\*/C IV ratios.

The equivalent width uncertainty outlined in §5 is exacerbated by the fact that the sum-of-blackbodies accretion disk spectrum has a long wavelength spectrum described by  $F_\nu \propto \nu^{1/3}$ . Such a steep spectrum is not generally seen in AGN; this is one of the problems hampering our understanding of accretion disks (e.g., Koratkar & Blaes 1999). Typical values of the optical to UV slope are observed to be around  $-0.5$  (e.g., Natali et al. 1998; Vanden Berk et al. 2001) to  $-0.3$  (e.g., Francis et al. 1991; Selsing et al. 2015). For SEDs with the same value of  $F_\lambda$  at 911Å, the continuum will be 7.87 times weaker at 10830Å for a  $F_\nu \propto \nu^{1/3}$  continuum than for a  $F_\nu \propto \nu^{-0.5}$  continuum. Therefore, we increase the upper limit on the allowed equivalent widths by a factor of 7.87.

The results are shown in Fig. 3 and Fig. 5. These two SEDs ( $r_{in} = 3.5r_g$ , and Schwartzschild) produce results that are very similar to those obtained with the harder SED explored in §5.1. This is not surprising given the large fraction of photoionizing flux in the extreme UV and the flat values of  $\alpha_{ox}$ . Specifically, they predicted only very low values of He I\*/C IV, and cannot explain the high value observed in Mrk 231.

### 5.3. Cloudy Models using the PHL 1811 Continuum

We again used the He I\*/P $\beta$ , P $\alpha$ /P $\beta$ , and He I\*/C IV ratio constraints, as in § 5.1 and § 5.2, but instead of using equivalent width, we normalized the SED to the Leighly et al. (2014) intrinsic continuum, and required the simulations to produce the observed He I\* flux. Note that we first deredden the He I\* flux using the inferred circumstellar reddening curve from Leighly et al. (2014). A large fraction of the simulations are able to meet these selection criteria, and their properties are shown in Fig. 3 and Fig. 5.

Fig. 3 shows that the He I\*/P $\beta$ , and P $\alpha$ /P $\beta$  ratios rather strongly resemble those produced by the soft SED considered in § 5.1. What is different is the He I\*/C IV ratio, which is higher than for the other SEDs and is consistent with the observed value from PHL 1811. This is not surprising as the very X-ray weak SED has been shown to

produce weak high-ionization lines (Leighly et al. 2007b). At the same time, the He I\*/C IV ratio does not approach the very high value exhibited by Mrk 231. As PHL 1811 is intrinsically exceptionally X-ray weak (Leighly et al. 2007a), with exceptionally small C IV equivalent width (Leighly et al. 2007b), we suspect that it would be difficult to produce a much higher ratio intrinsically, given our constraints on the line emission. This is further evidence that the He I\*/C IV ratio in Mrk 231 is high because of reddening, and is not intrinsic, and it seems likely that the UV continuum and broad-line region in Mrk 231 are likely not seen directly at all.

## 6. Discussion

### 6.1. Summary

We used observed emission lines from Mrk 231 and a comparison sample to investigate the binary-black hole model proposed by Yan et al. (2015), and to compare it with the circumstellar absorption model proposed by Leighly et al. (2014). We used infrared lines, which are subject to minimal reddening regardless of the model. The He I\* $\lambda$ 10830 line yielded information about the ionization parameter, while the P $\beta$  line at 12818Å and the P $\alpha$  line at 18751Å yielded information about the density (due to thermalization at high density) and column density of the emitting gas. C IV $\lambda$ 1548,1551 was used to probe the ultraviolet, to see whether that emission line is intrinsically weak and minimally absorbed, as proposed by Yan et al. (2015), or dramatically absorbed, as proposed by Leighly et al. (2015).

The Yan et al. (2015) model assumed that the broad line region emission in Mrk 231 is powered by the photoionizing continuum produced by thin-disk accretion onto the smaller of the two black holes. Thus, in order to produce emission lines in the near infrared that have typical equivalent widths with respect to the observed continuum, the equivalent widths with respect to the continuum produced by smaller black hole would have to be huge, approximately 100 times larger than normal, since the photoionizing continuum extrapolated into the infrared is  $\sim 100$  times weaker than the observed continuum (§3.2). This seems quite implausible, even without quantitative analysis, and thus is the first piece of evidence that the

Yan et al. (2015) model is untenable.

We followed with analysis using the photoionization code *Cloudy*. We first established that we were able to produce the observed He I\* equivalent widths, and He I\*/P $\beta$ , P $\alpha$ /P $\beta$ , and He I\*/C IV ratios of a comparison sample of objects using two spectral energy distributions that roughly bracket the properties of observed quasar continua. We next investigated spectral energy distributions similar to those proposed by Yan et al. (2015), i.e., sum-of-blackbodies accretion disks with small inner radii ( $r_{in} = 3.5r_g$  and Schwarzschild) that were normalized to the observed far-UV spectrum. Unlike the Yan et al. (2015) model, we required the X-ray portion of the spectrum to go through the observed spectrum presented by Teng et al. (2014). Mrk 231 was observed to have a rather typical He I\*/P $\beta$  ratio, so we searched among simulations that produce a typical range of He I\*/P $\beta$  ratios to see if any were able to produce the observed intensity of the He I\* emission line. There were none, even if the broad line region is assumed (unrealistically) to fully cover the continuum emitting source. This provided the second piece of evidence that Yan et al. (2015) model is untenable.

The final piece of evidence is He I\*/C IV ratio, which is observed to be very high in Mrk 231. Our *Cloudy* models show that this ratio is very sensitive to the spectral energy distribution. This is not surprising given that C IV is a high-ionization line and a major coolant, and it has been shown to be weak in the weak-line quasar PHL 1811 as a consequence of its intrinsically X-ray weak spectral energy distribution (Leighly et al. 2007b). Our simulations, using the PHL 1811 continuum, were able to reproduce the observed high He I\*/C IV ratio in PHL 1811. However, the He I\*/C IV ratio in Mrk 231 was observed to be  $\sim 100$  times higher. We concluded that we do not see the direct C IV emission in Mrk 231. The origin of the emission that we do observe is not known; we speculate it may be due to scattering (§6.6), or it may be produced in the BAL outflow (Veilleux et al. 2013).

## 6.2. Suggestive Results Regarding the Near Infrared Emission Lines

The focus of this paper is a critique of the Yan et al. (2015) model, and we do not purport to provide a full model of the broad line region.

Nevertheless, we have learned a few interesting things about the infrared lines and *Cloudy* models for them. The observed P $\alpha$ /P $\beta$  line ratios in the comparison sample are rather low, with a range between 0.94 and 1.74 and a mean of 1.2. They are much lower than the Case A (Case B) values of 2.33 (2.28) in the low density limit (Osterbrock & Ferland 2006). This suggests that the hydrogen-line emission regions are very optically thick and thermalization is important. This is not unexpected, as it has been known for many years that the Ly $\alpha$ /H $\beta$  is observed to be typically around 10, rather than 23 or 34 (the low and high density Case B limits; Osterbrock & Ferland 2006). It was surprising, however, to see how thermalization influences line ratios at different densities to produce a strongly localized density range for the simple one-zone model. While arguably not directly applicable to AGN spectra, it may be useful to consider this behavior for complete models of the broad line region.

Also intriguing is the sensitivity of the He I\*/P $\beta$  ratio to the spectral energy distribution. On the face of it, this result was not surprising, given that the He I\* line responds to the strength of the helium continuum, while the P $\beta$  depends principally on the column density of the gas. It suggests that the near-infrared broad line ratios could be used to infer the intrinsic spectral energy distribution of obscured quasars. But this result must be viewed with extreme caution. In this paper, we used a one-zone model for simplicity, and it is not clear that the same effect would be present in an extended-BLR model. Indeed, it is not clear that these lines can be trivially modeled using an extended-BLR model. Ruff et al. (2012) investigated an LOC model for the hydrogen lines, and found themselves forced into a small region of photoionization parameter space. This could be because the standard LOC, which was historically proposed to explain the high-ionization UV lines (Baldwin et al. 1995), is simply more appropriate for that regime, and less appropriate for the low-ionization lines considered here. In fact, the LOC doesn't always work well for high-ionization lines (Dhanda et al. 2007). In addition, the standard LOC has a large fraction of optically thin clouds, while we have shown that high optical depths are needed to produce sufficient line emission and correct line ratios. Moreover, it is



not clear that the SED that illuminates the gas emitting low-ionization lines is the same as the continuum we see; it may have been “filtered” by gas producing the high-ionization lines (Leighly 2004). Alternative models using radiation pressure confinement may work better for these lines (Baskin et al. 2014). While this is an interesting and potentially important problem given the dearth of SED diagnostics the infrared, it is beyond the scope of the present paper.

### 6.3. Powering the Mid-Infrared Continuum

While we have demonstrated that the strength of the near-IR broad-line emission cannot be accounted for by the UV-to-optical SED as observed and implies an intrinsically much more luminous ionizing continuum, there is an additional argument to be made based on considerations of the mid-infrared power of Mrk 231 that is independent of the physics of the broad-line region. The thermal near- and mid-infrared (2–20  $\mu\text{m}$ ) emission of quasars is attributed to dust heated by absorbing optical through X-ray emission from the central accretion disk. The tight, linear correlation between unobscured optical (0.1–1 $\mu\text{m}$ ) and infrared (1–100  $\mu\text{m}$ ) quasar luminosities seen in radio-quiet quasars supports this interpretation (e.g., Gallagher et al. 2007). The infrared luminosity is therefore arguably a more robust indicator of bolometric luminosity than the optical-UV as observed because the infrared is much less susceptible to dust extinction. Gallagher et al. (2007) recommended the 3 $\mu\text{m}$  luminosity in particular as a good single luminosity for estimating quasar bolometric luminosities because the hottest dust is certainly powered by the AGN with no starburst contamination. The weak PAH emission seen in the  $L$ -band and mid-infrared spectra of Mrk 231 supports the claim that this region of the spectrum is dominated by the quasar (Imanishi et al. 2007; Weedman et al. 2005). From the  $L$ -band spectrum of Mrk 231 presented in Imanishi et al. (2007), the  $L_{3\mu\text{m}}$  is  $7.5 \times 10^{44}$  erg s $^{-1}$ . Using the 3 $\mu\text{m}$ -to-IR bolometric correction of  $3.44 \pm 1.68$  (Gallagher et al. 2007) gives  $L_{\text{IR}} = (3.86 \pm 1.26) \times 10^{45}$  erg s $^{-1}$ . This is more than an order of magnitude *greater than* the 0.1–1 $\mu\text{m}$  luminosity of the observed continuum (gray dashed + green dashed continua) shown in Figure 2:  $L_{\text{opt,obs}} = 2.1 \times$

$10^{44}$  erg s $^{-1}$ . Correcting for SMC extinction with  $E(B - V) = 0.1$  following Yan et al. (2015) brings  $L_{\text{opt,obs}}$  up to  $2.9 \times 10^{44}$  erg s $^{-1}$ , still well below the  $L_{\text{IR}}$  that is supposedly powered by this continuum. However, the extinction-corrected 0.1–1.0 $\mu\text{m}$  continuum (orange dashed line in Fig. 2) gives  $L_{\text{opt}} = 2.7 \times 10^{45}$  erg s $^{-1}$ , in line with the expectations from the IR power (from Figure 2 of Gallagher et al. 2007).

### 6.4. Polarization

Another problem with the Yan et al. (2015) model is that it does not adequately explain the near-UV-to-optical polarization in Mrk 231: significant and strongly rising to the blue through  $\sim 3000\text{\AA}$  (Smith et al. 1995). This kind of polarization signature is commonly seen in reddened objects. Wills et al. (1992) presented an analysis of the similarly-polarized infrared-luminous quasar IRAS 13349+2438. They showed that electron scattering, which produces a wavelength-independent polarization, combined with a reddened continuum, produces a blue-polarized spectrum. That is, the intrinsic polarization is constant, but appears to increase toward the blue due to dilution by the unpolarized, reddened, direct continuum in the red. Alternatively, or in addition, scattering by small dust grains produces polarization increasing toward the blue (Rayleigh scattering). A similar polarization signature is seen among many Type 1 reddened objects (e.g., Smith et al. 2000; Schmid et al. 2001; Hines et al. 2001; Smith et al. 2002b,a, 2003). Mrk 231 is a low-ionization broad absorption line quasar, and these objects are known to be significantly polarized (e.g., Hines & Wills 1995; Ogle et al. 1999; Schmidt & Hines 1999; Brotherton et al. 2001; DiPompeo et al. 2011) and reddened (e.g., Reichard et al. 2003; Dai et al. 2008; Krawczyk et al. 2015). In addition, Mrk 231 shows evidence for X-ray absorption (Teng et al. 2014), and polarized Type 1 objects are more likely to suffer X-ray absorption than unpolarized ones (Leighly et al. 1997).

### 6.5. Strategic Absorption

Yan et al. (2015) noted that Mrk 231 has strong optical Fe II emission (i.e., flux), and therefore might be expected to have comparably strong UV Fe II emission, which is not seen.

The Leighly et al. (2014) circumstellar absorption model explains this lack of strong UV Fe II naturally via reddening; both the continuum and the line emission are attenuated in the near UV (Fig. 2). Since the Yan et al. (2015) model assumes that reddening is minimal, they needed to find another explanation for the weak UV Fe II flux. They proposed that since Mrk 231 is a known Fe II absorption line quasar (FeLoBAL), the Fe II emission is absorbed exactly by the Fe II absorption in the BAL outflow. This idea is untenable for several reasons. First, the velocity offset of the low-ionization line absorption in Mrk 231 is known to be between about  $-5,500$  and  $-4,000$  km s $^{-1}$  (e.g., Figure 8 in Leighly et al. (2014)). Yan et al. (2015) required a much broader velocity width to produce their exact subtraction, between  $-8,000$  and  $-1000$  km s $^{-1}$ . It is not clear that they would have obtained the same result using a realistic outflow profile.

More importantly, however, the recent *HST* STIS observation (which appears very similar to the spectrum shown in Fig. 2, albeit with the significant advantage of better signal-to-noise ratio and resolution) shows that Mrk 231's near-UV Fe II absorption is strong and saturated from low-excitation levels between 0 and 0.12 eV (near 2600 and 2400 Å), while absorption from higher excitation levels between 0.98 and 1.1 eV (near 2750Å) is weaker. If the weak, apparently unsaturated 275Å feature is correctly identified as high-excitation Fe II (rather than high-velocity Mg II), these lines might be produced in the narrow range of density between which they are predicted to appear and saturate (Lucy et al. 2014, Section 5.2). Regardless, the weakness or absence of these high-excitation Fe II lines supports the relatively low density range of the absorber inferred by Leighly et al. (2014). Whether or not this is true requires detailed analysis, beyond the scope of this paper.

### 6.6. Speculations on the Nature of the Far UV Emission in Mrk 231

This paper establishes what the far UV emission in Mrk 231 is not: it is clearly not the continuum emission of a small black hole in the binary black hole scenario proposed by Yan et al. (2015). So, then, what is it? While a detailed analysis is beyond the scope of this paper, we suggest that

a scattering scenario may have been too hastily dismissed by Veilleux et al. (2013). The continuum flux near 2000Å is found to be about 165 times weaker than the intrinsic continuum inferred by Leighly et al. (2014), i.e., 0.6% of the intrinsic flux. Such a level of scattering is not implausible; e.g., a median scattering efficiency of 2.3% is found in a sample of obscured quasars (e.g., Obied et al. 2015, although the scattering regions in those galaxies are very large). A scattering origin may explain the unusual UV emission lines, since it may be that only part of the BLR is mirrored by the scatterer. Or they may be produced in the outflow, as suggested by Veilleux et al. (2013). Veilleux et al. (2013) dismiss scattering due to the low level of polarization in the UV, as observed by Smith et al. (1995), but we note that while the polarization in the UV is lower than it is in the near-UV, it is not zero. Moreover, it shows a position angle rotation compared with the strong near-UV polarization, which suggests a different origin. Also, we note that the degree of polarization that is observed depends on the asymmetry of the scatterer; if largely spherically symmetric, high polarization is not expected. Finally, the optical polarization in Mrk 231 has been observed to be variable (Gallagher et al. 2005), and the *HST* UV polarization observation was performed more than 20 years ago.

KML acknowledges useful conversations with Dick Henry. KML thanks Erin Cooper for processing the Mrk 231 spectra. KML acknowledges support through STScI HST-GO-14058.001-A. SCG thanks the Natural Science and Engineering Research Council of Canada for support.

*Facilities:* IRTF (SpeX)

### REFERENCES

- Baldwin, J., Ferland, G., Korista, K., & Verner, D. 1995, ApJ, 455, L119
- Baskin, A., Laor, A., & Stern, J. 2014, MNRAS, 438, 604
- Bentz, M. C., Denney, K. D., Grier, C. J., et al. 2013, ApJ, 767, 149
- Bottorff, M., Ferland, G., Baldwin, J., & Korista, K. 2000, ApJ, 542, 644

- Brotherton, M. S., Arav, N., Becker, R. H., et al. 2001, *ApJ*, 546, 134
- Casebeer, D. A., Leighly, K. M., & Baron, E. 2006, *ApJ*, 637, 157
- Crenshaw, D. M., Kraemer, S. B., Bruhweiler, F. C., & Ruiz, J. R. 2001, *ApJ*, 555, 633
- Dai, X., Shankar, F., & Sivakoff, G. R. 2008, *ApJ*, 672, 108
- Denney, K. D., De Rosa, G., Croxall, K., et al. 2014, *ApJ*, 796, 134
- Dhanda, N., Baldwin, J. A., Bentz, M. C., & Osmer, P. S. 2007, *ApJ*, 658, 804
- Dietrich, M., Hamann, F., Shields, J. C., et al. 2002, *ApJ*, 581, 912
- DiPompeo, M. A., Brotherton, M. S., & De Breuck, C. 2011, *ApJS*, 193, 9
- Farrah, D., Afonso, J., Efstathiou, A., et al. 2003, *MNRAS*, 343, 585
- Ferland, G. J., Porter, R. L., van Hoof, P. A. M., et al. 2013, *Rev. Mexicana Astron. Astrofis.*, 49, 137
- Francis, P. J., Hewett, P. C., Foltz, C. B., et al. 1991, *ApJ*, 373, 465
- Frank, J., King, A., & Raine, D. J. 2002, *Accretion Power in Astrophysics: Third Edition*
- Gallagher, S. C., Brandt, W. N., Chartas, G., Garmire, G. P., & Sambruna, R. M. 2002, *ApJ*, 569, 655
- Gallagher, S. C., Richards, G. T., Lacy, M., et al. 2007, *ApJ*, 661, 30
- Gallagher, S. C., Schmidt, G. D., Smith, P. S., et al. 2005, *ApJ*, 633, 71
- Glikman, E., Helfand, D. J., & White, R. L. 2006, *ApJ*, 640, 579
- Goobar, A. 2008, *ApJ*, 686, L103
- Hamann, F., Kanekar, N., Prochaska, J. X., et al. 2011, *MNRAS*, 410, 1957
- Hines, D. C., Schmidt, G. D., Gordon, K. D., et al. 2001, *ApJ*, 563, 512
- Hines, D. C., & Wills, B. J. 1995, *ApJ*, 448, L69
- Imanishi, M., Nakanishi, K., Tamura, Y., Oi, N., & Kohno, K. 2007, *AJ*, 134, 2366
- Koratkar, A., & Blaes, O. 1999, *PASP*, 111, 1
- Korista, K., Baldwin, J., Ferland, G., & Verner, D. 1997, *ApJS*, 108, 401
- Krawczyk, C. M., Richards, G. T., Gallagher, S. C., et al. 2015, *AJ*, 149, 203
- Kriss, G. A., Peterson, B. M., Crenshaw, D. M., & Zheng, W. 2000, *ApJ*, 535, 58
- Kuraszkiewicz, J. K., Green, P. J., Crenshaw, D. M., et al. 2004, *ApJS*, 150, 165
- Kuraszkiewicz, J. K., Green, P. J., Forster, K., et al. 2002, *ApJS*, 143, 257
- Kwan, J., & Krolik, J. H. 1981, *ApJ*, 250, 478
- Landt, H., Bentz, M. C., Ward, M. J., et al. 2008, *ApJS*, 174, 282
- Laor, A., Bahcall, J. N., Jannuzi, B. T., et al. 1994, *ApJ*, 420, 110
- Leighly, K. M. 2004, *ApJ*, 611, 125
- Leighly, K. M., Cooper, E., Grupe, D., Terndrup, D. M., & Komossa, S. 2015, *ApJ*, 809, L13
- Leighly, K. M., Dietrich, M., & Barber, S. 2011, *ApJ*, 728, 94
- Leighly, K. M., Halpern, J. P., Helfand, D. J., Becker, R. H., & Impey, C. D. 2001, *AJ*, 121, 2889
- Leighly, K. M., Halpern, J. P., Jenkins, E. B., & Casebeer, D. 2007a, *ApJS*, 173, 1
- Leighly, K. M., Halpern, J. P., Jenkins, E. B., et al. 2007b, *ApJ*, 663, 103
- Leighly, K. M., Hamann, F., Casebeer, D. A., & Grupe, D. 2009, *ApJ*, 701, 176
- Leighly, K. M., Kay, L. E., Wills, B. J., Wills, D., & Grupe, D. 1997, *ApJ*, 489, L137
- Leighly, K. M., Terndrup, D. M., Baron, E., et al. 2014, *ApJ*, 788, 123

- Lucy, A. B., Leighly, K. M., Terndrup, D. M., Dietrich, M., & Gallagher, S. C. 2014, *ApJ*, 783, 58
- Natali, F., Giallongo, E., Cristiani, S., & La Franca, F. 1998, *AJ*, 115, 397
- Obied, G., Zakamska, N. L., Wylezalek, D., & Liu, G. 2015, *ArXiv e-prints*
- O'Brien, P. T., Reeves, J. N., Simpson, C., & Ward, M. J. 2005, *MNRAS*, 360, L25
- Ogle, P. M., Cohen, M. H., Miller, J. S., et al. 1999, *ApJS*, 125, 1
- Osterbrock, D. E., & Ferland, G. J. 2006, *Astrophysics of gaseous nebulae and active galactic nuclei*
- Pei, Y. C. 1992, *ApJ*, 395, 130
- Reichard, T. A., Richards, G. T., Hall, P. B., et al. 2003, *AJ*, 126, 2594
- Richards, G. T., Lacy, M., Storrie-Lombardi, L. J., et al. 2006, *ApJS*, 166, 470
- Riffel, R., Rodríguez-Ardila, A., & Pastoriza, M. G. 2006, *A&A*, 457, 61
- Ruff, A. J., Floyd, D. J. E., Webster, R. L., Korista, K. T., & Landt, H. 2012, *ApJ*, 754, 18
- Rupke, D. S. N., & Veilleux, S. 2011, *ApJ*, 729, L27
- Sanders, D. B., Soifer, B. T., Elias, J. H., Neugebauer, G., & Matthews, K. 1988, *ApJ*, 328, L35
- Schmid, H. M., Appenzeller, I., Camenzind, M., et al. 2001, *A&A*, 372, 59
- Schmidt, G. D., & Hines, D. C. 1999, *ApJ*, 512, 125
- Selsing, J., Fynbo, J. P. U., Christensen, L., & Krogager, J.-K. 2015, *ArXiv e-prints*
- Smith, J. E., Young, S., Robinson, A., et al. 2002a, *MNRAS*, 335, 773
- Smith, P. S., Schmidt, G. D., Allen, R. G., & Angel, J. R. P. 1995, *ApJ*, 444, 146
- Smith, P. S., Schmidt, G. D., Hines, D. C., Cutri, R. M., & Nelson, B. O. 2000, *ApJ*, 545, L19
- . 2002b, *ApJ*, 569, 23
- Smith, P. S., Schmidt, G. D., Hines, D. C., & Foltz, C. B. 2003, *ApJ*, 593, 676
- Steffen, A. T., Strateva, I., Brandt, W. N., et al. 2006, *AJ*, 131, 2826
- Teng, S. H., Brandt, W. N., Harrison, F. A., et al. 2014, *ApJ*, 785, 19
- Tilton, E. M., & Shull, J. M. 2013, *ApJ*, 774, 67
- Vanden Berk, D. E., Richards, G. T., Bauer, A., et al. 2001, *AJ*, 122, 549
- Veilleux, S., Trippe, M., Hamann, F., et al. 2013, *ApJ*, 764, 15
- Wang, L. 2005, *ApJ*, 635, L33
- Wang, T.-G., Lu, Y.-J., & Zhou, Y.-Y. 1998, *ApJ*, 493, 1
- Weedman, D. W., Hao, L., Higdon, S. J. U., et al. 2005, *ApJ*, 633, 706
- Wills, B. J., Wills, D., Evans, II, N. J., et al. 1992, *ApJ*, 400, 96
- Yan, C.-S., Lu, Y., Dai, X., & Yu, Q. 2015, *ApJ*, 809, 117